Robust Networks of Rainfall Extremes Emerge Despite Fragile Ocean Monsoon Causality Under Internal Variability

Hemant Poonia[1], Divya Upadhyay[1], Akshaya C. Nikumbh[2], Raghu Murtugudde[3] Udit Bhatia[1,4,5],

[1]Department of Civil Engineering, Indian Institute of Technology Gandhinagar, India
[2]Centre for Climate Studies, Indian Institute of Technology Bombay, Mumbai, India
[3]Emeritus Professor, University of Maryland, College Park, MD, United States of America and Indian Institute of Technology Bombay, Mumbai, India
[4]Department of Computer Science and Engineering, Indian Institute of Technology Gandhinagar, India
[5]Department of Earth Science, Indian Institute of Technology Gandhinagar, India

Abstract

Climate ready multi sectoral risk management relies on understanding not only where extreme rainfall occurs but also how such events synchronize across regions and interact with internal climate modes. The stability of synchronized rainfall networks and remote climate forcings under internal climate variability (ICV), especially when aggregating ensemble simulations for statistical robustness, remains poorly understood. Using a 50 member EC Earth3 large ensemble, we show the co-existence of robust and weak climate networks. Despite significant variability in regional rainfall intensities, extreme rainfall spatial synchronization patterns remain remarkably robust, driven by intrinsic atmospheric processes such as Rossby wave propagation. In contrast, slower teleconnections, notably from the El Niño Southern Oscillation and the Indian Ocean Dipole, exhibit marked variability under minor initial condition perturbations, often altering or reversing causal relationships. This fundamental asymmetry reveals the critical limitations of relying on deterministic or single member model outputs. Our findings advocate ensemble based frameworks to disentangle robust dynamical pathways from fragile ones, offering a more reliable foundation for climate projections, model evaluations, and sectoral resilience planning under uncertain climate futures.

Keywords: Rainfall Extremes, Network Analysis, Internal Climate Variability, Event Synchronization, Teleconnections

Introduction

The climate we observe represents only one realization among the countless possible trajectories, constrained by the dynamical and thermodynamical processes that govern the Earth's climate system with their underlying uncertainties [1]. Consequently, the characteristics of extreme climate events, such as the intensity, spatial extent, and frequency of extreme rainfall, can vary substantially across equally plausible climate trajectories. This variability complicates risk assessment and decision making in a range of climate-sensitive sectors, including agriculture, water management, energy systems, transportation, buildings, public health, and infrastructure [2–5]. Fundamentally, it challenges our dependence on historical data or single-simulation projections to estimate future risks from extremes.

However, this complexity also presents a significant scientific opportunity. Using large ensembles of climate simulations initiated from slightly varied Initial Conditions (ICs), known as Single-Model Initial-condition Large Ensembles (SMILEs), allows systematic exploration of numerous potential climate trajectories. Such ensemble simulations enable quantification of internal climate variability (ICV), the natural variability arising from internal interactions within the climate system, and thus improve the characterization of uncertainty inherent in extreme event projections. Although engineering practice, infrastructure planning, and other sectoral applications commonly use intensity - duration - frequency (IDF) and depth - duration - frequency (DDF) curves derived from historical data or individual model runs [6], these benchmarks embed deep uncertainties from ICV, model structure, and scenario assumptions [7]. During the past decade, SMILEs have proven invaluable in disentangling externally forced signals from internal variability, revealing that unforced fluctuations alone can match or even exceed anthropogenic trends in regional precipitation extremes [7–9]. While attribution studies reliably detect anthropogenic fingerprints in extreme rainfall shifts, these typically focus on bulk statistics (e.g., return periods), often neglecting how internal variability amplifies or masks local signals crucial for infrastructure planning. Explicitly linking attribution outcomes to variability across ensemble members can thus enhance understanding of when anthropogenic signals dominate and when internal variability prevails.

Small perturbations in initial ocean-atmosphere states can develop into significantly divergent precipitation trajectories, critically affecting the frequency, intensity, and duration of extreme events [1, 10]. Understanding whether large-scale teleconnections and physical mechanisms organizing these extremes remain robust across ensemble members is therefore essential before applying IDF/DDF projections or making sectoral planning decisions based on pooled climate realizations. The pooling of precipitation extremes across multiple ensemble members is commonly employed to improve the sampling of rare events and construct more robust estimates of tail statistics [6, 7]. This approach is useful for characterizing the distribution of outcomes arising from ICV. However, such a pooling often implicitly assumes that large-scale teleconnections linking climate drivers, such as the El Niño Southern Oscillation (ENSO) or the Indian Ocean Dipole (IOD), to regional rainfall remain stable across ensemble members. In practice, ICV can modulate the strength, spatial footprint, or even directionality of these teleconnections, leading to changes in the underlying physical mechanisms and their timing. Consequently, aggregating extremes across ensemble members without first evaluating the robustness of these causal pathways can obscure key sources of uncertainty. Explicitly assessing teleconnection stability under ICV is therefore essential before using pooled ensemble statistics for infrastructure risk analysis or climate adaptation planning.

Despite increasing recognition of the importance of ICV in massive extreme event statistics, the spatiotemporal organization of rainfall extremes - their clustering, synchronization, and cascading impacts across regions - remains understudied [11, 12]. Such spatial and temporal structures significantly shape the likelihood of compound impacts, with direct consequences for the resilience of sectors such as infrastructure, agriculture, energy, and health systems. Recent studies underscore the considerable uncertainty introduced by ICV in return-period estimates of extreme rainfall [6, 7, 13–15]. However, these analyses have largely overlooked how internal variability affects the spatio-temporal coherence of extreme events.

Recent complex network analyzes have begun to address this gap by revealing how atmospheric pathways such as monsoonal circulations [16, 17] and Rossby wave trains [18–20] synchronize extreme rainfall events (ERE) in geographically distant regions. However, these studies typically rely on single memeber realizations or observational records, limiting their ability to fully characterize how ICV plays a role or perturbs these synchronization patterns [17, 20, 21]. Furthermore, causal inference methods, although increasingly applied in multi-model climate assessments [22–24], are yet to be systematically employed to evaluate teleconnections under internal variability. Overreliance on limited realizations can result in inconsistent evaluations and rankings of climate models, potentially skewing infrastructure design guidelines and flood-risk management strategies.

In this study, we explicitly address these critical scientific gaps by systematically investigating the robustness of network derived synchronization structures of extreme rainfall across multiple initial-condition ensemble members. Specifically, we evaluate whether the synchronization of extreme rainfall events, captured by complex network methods, remains stable under ICV. In addition, we explore whether atmospheric mechanisms primarily drive these synchronization patterns and how their relative influence is modulated by internal variability. Finally, we apply causal-inference techniques between ensemble members to determine whether established teleconnections, such as those linking ENSO and IOD to Indian summer monsoon rainfall, retain their directional relationships under ICV. By integrating network-based synchronization metrics with causal inference, our study explicitly reveals how ICV reshapes both the spatial structure and the underlying dynamical mechanisms driving extreme rainfall synchronization.

Results

Variability in Spatial Patterns and Extremes across Ensemble Members

Accurate projections of the hydroclimate for decision horizons or decadal timescales are crucial for engineering design, but ICV can drive large deviations in the mean and extremes of precipitation, even under identical external forcings [6, 25] Figure 1 compares two initial condition (IC) runs r10i1p1f1 and r12i1p1f1 from a EC Earth3 ensemble. Both runs share identical historical external forcings, but differ slightly in their initial atmospheric and oceanic states. Panels (a)–(d) depict mean precipitation changes from 1981-2010 to 1951-1980, revealing opposite signals of approximately + 65% and 30% in the regions of northern Australia, South Central Asia and the Amazon (marked by boxes). Such pronounced regional discrepancies underscore how minor variations in initial atmospheric and oceanic states can evolve into markedly divergent decadal scale hydroclimatic trajectories. These results align closely with previous large ensemble analyses that demonstrate a strong regional precipitation sensities to ICV [1, 25].

To examine whether similar discrepancies extend to extreme rainfall intensities relevant for infrastructure design, panels (e)–(f) in Figure 1 show Intensity–Duration–Frequency (IDF) curves for return periods of 30, 50, and 100 years, aggregated across all 50 members of the ensemble. The interquartile range (IQR) for the 1-day, 100 year rainfall intensities reveals considerable variability: for example, South Central Asia exhibits variations of approximately 16 to 31 mm/day, while northern Australia vary over 4.5 to 9 mm/day. This wide uncertainty due solely to ICV poses significant challenges for engineering designs, which often assume stationarity and stable IDF benchmarks over typical 30 year planning horizons [7]. Our findings further confirm insights from earlier SMILE studies that ICV can rival or even surpass externally forced signals on decadal timescales, influencing both mean climate states and short duration rainfall extremes [6, 7, 25].

Given these clear impacts of ICV on the regional precipitation means and extremes, a critical additional question arises: Does the internal variability influence the spatial and temporal organization of extreme rainfall events in a similar way? We address this in the following subsection by analyzing the robustness and variability of synchronized extreme rainfall networks across ensemble members.

Robust Spatial Network of Synchronous Extreme Rainfall across ICs

Although Figure 1 illustrates considerable variability in the mean JJAS precipitation and short duration extremes across different initial conditions (IC) simulations of the EC Earth3 ensemble, it remains unclear whether extreme rainfall events in different regions continue to be organized by similar large scale atmospheric mechanisms. To diagnose this, Figure 2 examines whether synchronous extremes retain a coherent spatial structure under both historical baseline conditions (1980–2014) and a near future scenario (SSP245, 2015–2049), despite the divergent ensemble outcomes in event intensity and frequency.

We employ an event synchronization procedure (see Methods) that defines Extreme Rainfall Events (EREs) at each grid cell as the top 10% of wet days ($\geq$ 1 mm/day). Two grid cells are considered synchronized if their EREs occur within ±10 days of each other, a timescale chosen to capture traveling wave trains, monsoonal circulations, and other large scale circulation patterns known to synchronize heavy rainfall across large geographic distances [26, 27]. To minimize spurious linkages, we retain only synchronization links exceeding a 95th percentile significance threshold, determined through a reshuffling procedure (1000 reshuffles per grid cell, see Methods). The resulting binary, undirected synchronization network characterizes each grid cell (node) by its degree, defined as the number of other cells it synchronizes with. High degree nodes typically reflect regions influenced by persistent large-scale atmospheric forcings such as the monsoon belts and the Intertropical Convergence Zone (ITCZ) [20, 28, 29].

Panels (a) and (c) of Figure 2 present the spatial distribution of degrees for two representative IC runs under historical forcing. Despite notable differences in their mean and extreme precipitation magnitudes (Figure 1), both synchronization networks exhibit strikingly similar spatial patterns. Highest degree nodes consistently cluster along known monsoon corridors and the ITCZ, reinforcing that the spatial ”backbone” of synchronous rainfall is remarkably robust to initial state perturbations. The ±10-day synchronization window effectively filters out the short lived convective or mesoscale systems, highlighting broader, persistent atmospheric dynamics that facilitate extensive rainfall synchronization. These observations suggest that, although the exact timing, intensity, and frequency of extremes differ among ensemble members, the underlying spatial organization driven by large scale atmospheric processes remains largely invariant with continued warming.

Panels (b) and (d) of Figure 2 illustrate these synchronization patterns for the same IC runs under the SSP245 scenario, highlighting the changes relative to the historical baseline. The regions initially exhibiting moderate to high degrees tend to become more interconnected under modest warming, indicating an expansion of synchronous extreme rainfall episodes. Importantly, this enhanced synchronization does not translate uniformly into higher local rainfall intensities everywhere. Rather, it underscores the persistence and the potential intensification of large-scale dynamical structures that synchronize extreme rainfall events. Statistical analyzes, including Kolmogorov-Smirnov tests and the low Jeffrey divergence scores, confirm that the degree distributions remain remarkably similar across the different IC runs, reinforcing the network topology robustness against internal variability and moderate forced climate changes. This stability provides a strong justification for pooling multiple IC realizations to improve sampling of the rare synchronized extremes, since the fundamental spatial linkages appear to be largely unaffected by the ICs or moderate warming scenarios.

To explicitly isolate the influence of ICV, we apply the event synchronization procedure to a 35 year subset of the preindustrial control (piControl) simulation. The resulting network provides a spatial degree baseline devoid of external anthropogenic forcing (Supplementary Figure S1). Although anthropogenic warming modifies the absolute density and spatial reach of synchronization links, the piControl baseline clearly indicates that core connectivity patterns primarily emerge from intrinsic internal climate dynamics rather than externally forced changes.

One possible reason for this remarkable spatial invariance is that, to the first order, the statistics of the extreme rainfall event frequencies constrain the network topology itself. When grid cells experience similar numbers of extreme events across different IC runs, pairwise-synchronization links naturally coalesce into nearly identical spatial structures. This hypothesis is supported by the low variability in extreme event frequencies observed throughout the historical ensemble (Supplementary Fig. S2), suggesting that the minimal spread in the event count alone is sufficient to stabilize the connectivity structure.

Having established that the spatial organization of synchronous extreme rainfall remains robust under internal variability, we now investigate whether the large-scale atmospheric teleconnections that underpin such synchronizations patterns remain consistent across ensemble members. For this we use Examples of South central Asia, Europe and South East Europe and South China case study as motivating examples, since these regions are known to face near simulatneous extreme rainfall events.[20, 30]

Persistent Silk Road Teleconnection Linking Europe and South Central Asia

Quasi-stationary Rossby wave trains strongly influence synchronous extreme rainfall across large geographic domains. Although such teleconnections are extensively documented, their robustness to ICVs, particularly across multiple ensemble realizations, remains unclear. Investigating this robustness is essential for improving the predictability of rainfall extremes and guiding region specific climate adaptation strategies. Here, we specifically analyze the stability of the Silk Road teleconnection, a well established midlatitude wave pattern that connects extreme rainfall events (EREs) between Europe and South Central Asia during the boreal summer [31–33]. Understanding this teleconnection is particularly crucial due to its implications for the monsoonal rainfall variability and the associated flood risks in densely populated regions.

To examine the teleconnection robustness, we define daily EREs as rainfall exceeding the local 90th percentile, smoothed using a 10 day low pass filter to capture persistent synoptic scale rainfall anomalies. We computed the lead-lag ranked correlations of the extremes of rainfall between Europe (42 ° N - 50 ° N, 3 ° E - 15 ° E) and South Central Asia (SCA) in 50 initial condition (IC) runs of the EC Earth3 ensemble. In particular, peak correlations occur consistently within a narrow 1–3 day window (Figure 3a), highlighting the temporal stability of the interdependence of the EREs in two selected regions. This consistent lag implies that, while the internal variability strongly affects local rainfall magnitudes, it does not significantly disrupt the underlying atmospheric mechanisms enabling synchronized rainfall events across distant regions.

Composite analyses of rainfall anomalies (relative to JJAS climatology) further confirm the peak rainfall extremes in Europe typically precede intensified rainfall in South Central Asia by approximately three days, as demonstrated for representative IC runs (r105i1p1f1 shown in Fig. 3b–e; r113i1p1f1 in Supplementary Fig. S3). Concurrent anomalies in 250 hPa meridional winds (Figure 3 d-e) illustrate an eastward propagating Rossby wave train, characteristic of the Silk Road pattern. Spectral analysis consistently reveals a dominant wave number 6 across ensemble members, reinforcing that this synoptic scale structure is resilient to internal variability.

Across all the 50 members of the initial condition EC Earth, the frequency analysis shows that the synchronization between the European and South Central Asian (SCA) rainfall extremes peaks from mid-July to the end of August (Fig. 4a). When the Most Synchronization Days (MSDs) are conditioned on phases of the Indian Summer Monsoon (ISMR), synchronization is strongest during active monsoon periods (Fig. 4b–c), when enhanced upper-level Rossby-wave activity overlaps with deep monsoon convection.

A similar response has been noted in previous studies [33–35]. Upper level anticyclonic anomalies near the North Atlantic jet exit region trigger a stationary Rossby wave response, which in turn enhances the downstream Central Asian High. This high influences monsoon convection through two key pathways: it redirects the Rossby wave equatorward, intensifying convection over northern India [33], and active convection over this region further reinforces the Central Asian High via the monsoon desert mechanism [36].

We further verified intraseasonal synchronization using an Asian Summer Monsoon (ASM) focused case study, applying exactly the same composite methodology and extracting MSDs as in our Europe–SCA analysis. We examined the interdependence of EREs between South-East Europe (39°–47° N, 15°–29° E) and South China (24°–30° N, 105°–118° E)—a pair motivated by the near simultaneous early summer 2018 extremes in SE Europe and the Meiyu/Baiu sector [30]. The resulting composites (Supplementary Fig. S4(a)) reproduce the expected seasonal evolution with more synchronizations in June followed by a decreasing trend, with a recognizable shift from an upper level zonal flow east early in the season to a westward flow later (over Japan in particular). This transition is consistent with the end of the Meiyu/Baiu, marked by the weakening of high-altitude westerly jets and the emergence of easterlies over the same region [37]. In addition, upper-level meridional wind anomalies confirm a Rossby-wave linkage between these mid-latitude regions, supporting the interpretation that wave propagation organizes remote ERE synchronization [20, 33]. Overall, temporal ordering and upper tropospheric conditions are mutually consistent with observed connections, and the same qualitative behavior recurs across all 50 EC-Earth initial-condition members (see Supplementary Fig. S4), underscoring the robustness of this result.

our results thus consistently identify the Silk Road teleconnection as a persistent dynamical pathway that synchronizes rainfall between Europe and South Central Asia (SCA) and, in the ASM case study, reveal an upper-level circulation link between South East Europe and South China, the extent to which ICV modulates the strength, spatial footprint, and reliability of these links remains uncertain. In particular, slower oceanic feedbacks may systematically reinforce or disrupt these atmospheric connections under different climate regimes. Clarifying these interactions is essential for understanding the dynamical basis of rainfall synchronization. We therefore proceed to a causal analysis of oceanic modes and their links to Indian Summer Monsoon Rainfall (ISMR) across multiple realizations of ICV.

Fragile Ocean Indian Summer Monsoon Rainfall Teleconnections under Internal Climate Variability

Although our previous analyses revealed that spatial and atmospheric teleconnections exhibit robustness across multiple initial condition (IC) ensemble runs, the stability of ocean driven teleconnections to Indian Summer Monsoon Rainfall (ISMR) under ICV remains uncertain. Given the longer memory and complex interactions of oceanic modes compared to the atmospheric drivers, ocean–monsoon coupling pathways may be especially susceptible to small initial perturbations. To systematically evaluate this hypothesis, we applied a lagged causal inference framework (PCMCI +, see Methods) to assess the consistency of canonical ocean Monsoon teleconnections, such as ENSO-to-ISMR, across multiple ICs.

We constructed monthly climate mode indices for major oceanic drivers: El Niño Southern Oscillation (ENSO; NINO3.4 index), Indian Ocean Dipole (IOD), Atlantic Multidecadal Oscillation (AMO), Pacific Decadal Oscillation (PDO), North Atlantic Oscillation (NAO), Atlantic Niño (ATLNINO), and ISMR itself. Monthly anomalies were calculated from observational datasets (COBE SST anomalies and IMD rainfall, 1871–2014) and eight historical members of the IC ensemble of EC Earth3 (1850–2014). PCMCI+ identifies statistically significant lagged causal links via partial correlation tests with a maximum lag of five months, selected to encompass relevant seasonal ocean–monsoon interactions.

Observational data reproduce well established teleconnections (Fig. 5a), particularly the robust ENSO driven ISMR variability and strong ENSO–IOD coupling, with AMO modulating the IOD. However, individual IC runs exhibit striking differences in their causal network structures (Fig. 5c). Some IC realizations yield extensive ocean to monsoon causal linkages, whereas others produce sparse or basically no connections. This variability arises because slow evolving oceanic modes diverge rapidly among ensemble members, shifting phases and amplitudes enough to substantially alter teleconnection strengths. Consequently, relying on the realizations of a single model risks misinterpreting weak or strong ocean–ISMR relationships as inherent physical characteristics rather than resulting from internal variability.

To further highlight how internal variability modulates the strength of ocean monsoon coupling, we analyzed the node degree time series of causal networks derived from PCMCI+ across eight historical IC members of EC Earth3 using simple Pearson correlations (Supplementary Figure S5). Realizations maintaining persistent ENSO→ISMR and IOD→ISMR causal links exhibit consistently high correlations between climate modes, indicating stable teleconnection structures. In contrast, ICs with intermittent or absent links display weaker fragmented correlations, reflecting episodic decoupling between the ocean modes and the monsoon rainfall. This analysis underscores that ICV not only determines the presence or absence of specific teleconnections but fundamentally affects the coherence and consistency of large scale coupling patterns.

To robustly quantify Ocean–ISMR teleconnections despite ICV induced variability, we employ a multipleinitial condition ensemble approach (MICE). By concatenating data across multiple IC runs, MICE reliably recovers the principal ocean to monsoon causal pathways observed historically (Fig. 5b). Bootstrap aggregation methods applied within this ensemble context distinguish robust teleconnections from spurious IC dependent artifacts, clearly demonstrating the advantage of ensemble aggregation. Specifically, ensemble members characterized by prolonged weak ENSO and IOD epochs yield sparse causal networks, whereas IC runs with frequent, strong ENSO/IOD occurrences produce denser, more interconnected networks.

Collectively, these results strongly caution against assessing model fidelity or interpreting teleconnections robustness based solely on single realization of a model simulations. Our findings highlight the critical role of ensemble based frameworks, such as MICE combined with robust statistical aggregation, in accurately characterizing ocean atmosphere teleconnections. This ensemble perspective is essential for preventing misinterpretation of internal variability as fundamental physical uncertainty, thereby improving reliability in climate inference and improving decision making for climate adaptation.

Discussion and Conclusion

Decision making for climate risk management often implicitly assumes tha the historical climate records or single model simulations represent a reliable or comprehensive depiction of future extremes. However, the observed climate trajectory is merely one among the many plausible realizations, each shaped by ICV. While dynamical and thermodynamical constraints define the broad envelope of physically possible outcomes, ICV can still give rise to extremes that are surprising in their timing or location, even if not unexpected in a theoretical sense. Our study directly addresses this challenge by using a 50 member EC Earth3 ensemble to systematically examine how small perturbations in initial oceanic and atmospheric states influence regional precipitation patterns, extremes, and large scale teleconnections.

Our analysis yields two critical insights. First, even under identical external forcings, minor differences in ICs can lead to significantly divergent regional precipitation responses, affecting both mean and extreme rainfall. This internal variability fundamentally challenges the conventional assumptions of climate stationarity that underpin planning in multiple sectors, including agriculture, water management, energy systems, health, urban development, and infrastructure. Second, despite the pronounced spread in rainfall intensity between ensemble members, the spatial synchronization of EREs remains remarkably robust. Specifically, regions governed by persistent large scale atmospheric processes, such as monsoonal systems and the ITCZ, consistently exhibit coherent synchronization patterns, suggesting that the organizational dynamics of EREs are resilient to internal perturbations.

Mechanistically, our results reveal a sharp contrast between atmospheric and oceanic teleconnections under internal variability. The Silk Road teleconnection, a well known Rossby wave pathway linking EREs between Europe and South Central Asia, reliably emerges across ensemble members, reflecting the structural stability of upper tropospheric waveguides. In contrast, ocean driven teleconnections, such as ENSO–ISMR coupling, exhibit marked sensitivity to ICV, varying significantly in strength, directionality, and spatial imprint across initial condition runs. This contrast highlights the fragility of slower evolving oceanic processes and the resulting uncertainty in their causal influence on regional rainfall.

These findings have immediate implications for the multi sectoral assessment of climate risk and the design of resilient systems. The robustness of atmospheric synchronization networks strengthens the case for ensemble based diagnostics to inform more reliable estimation of extreme event probabilities, critical for sectoral planning in agriculture, disaster risk reduction, public health, energy, and infrastructure. In contrast, the instability of ocean–monsoon teleconnections underscores the limitations of relying on single realizations or short observational records to inform long term strategies. Ensemble frameworks, combined with causal inference and statistical aggregation, offer a pathway to more robust and adaptive climate informed decision making.

Our approach has limitations, including incomplete upper level wind data for validating wave structures, potential methodological biases that favor large scale signals, and limited exploration of nonlinear causal inference techniques. However, by disentangling robust atmospheric pathways from more variable ocean driven pathways, our results reinforce the value of large ensemble methodologies for understanding the structural organization of climate extremes.

Finally, despite the growing availability of open source Earth System Model products, which now extend to hundreds of petabytes, significant challenges remain in translating these data into actionable insights. Current practices still often rely on limited observational records or deterministic model output, potentially overlooking key aspects of ICV . Our findings directly contribute to addressing this gap by demonstrating the practical value of ensemble based approaches in quantifying uncertainty and identifying robust teleconnections. The widespread adoption of such frameworks can significantly enhance the scientific foundation for climate projections and support informed multi sectoral adaptation planning in the face of an increasingly uncertain climate future.

Methods

Data

Daily precipitation and wind components at 250 hpa are obtained for 50 members of the initial conditions ensemble of the CMIP6 EC Earth3 model, available through the Earth System Grid Federation (https://esgf-data.dkrz.de/projects/esgf-dkrz/). These include simulations from the historical experiment covering 1980-2014 and the SSP245 scenario from 2015-2049. This large single model initial condition ensemble (SMILEs) enables us to assess the robustness of event synchronization networks under internal variability and near term climate change. We used observational data from the Multi-Source Weighted Ensemble Precipitation (MSWEP) V2.2 dataset for the period 1980 2014. This dataset merges gauge, satellite, and reanalysis data and is provided at a spatial resolution of 0.1° × 0.1° . We restrict our analysis in the meridional direction to the latitudinal range from the Southern subtropics to the Northern mid latitudes (180° W–180° E, 30° S–70° N).To ensure consistency in spatial analysis, we apply nearest neighbor interpolation using the Fekete algorithm, which redistributes the data onto approximately 26000 uniformly distributed spatial points. The spacing between these points corresponds to the equatorial distance on a Gaussian 1° grid.

All precipitation time series are linearly detrended prior to analysis. Wet days are defined as days with daily rainfall $\geq$ 1 mm/day. EREs at each location are then identified as days when the precipitation exceeds the 90th percentile of all wet days at that location. This study focuses on the analysis of EREs occurring within the monsoon season, set as June–September (JJAS). Consequently, the analysis is limited to this specific time frame.

The monthly rainfall data based on fixed stations from a long historical dataset of Parthasarathy [38](1871–2016) is used as a measure of ISMR. The SST fields, obtained from COBE SST2 [39] data (1850–2016), are used as the primary SST field for deriving monthly AMO and ENSO indices. The monthly atmospheric SLP fields are obtained from NCEP 20CR V3 [40]. Additionally, we used monthly SST and rainfall data from eight initial condition ensemble members of the EC Earth3 model spanning 1850-2014. These extended simulations are used to assess the robustness of ocean Indian monsoon causal relationships using the PCMCI+ algorithm. Both SST and rainfall time series are taken from the same ensemble members to preserve consistency between oceanic and atmospheric states during causal analysis.In this study, our experimental design for testing the robustness of teleconnection and causal influence closely follows the design of Goswami etal. [23], ensuring comparability with the observation experiment.

Complex Network Analysis

Event Synchronization (ES)

Event Synchronization (ES) is a non parametric technique for detecting temporal dependencies between time discrete events, making no assumptions about linearity or stationarity. In this study, we employ ES to quantify how extreme rainfall events (EREs) synchronize across different geographical locations, following [17–20].

1. Identifying the dynamic temporal delay

For two grid points i and j, let their sets of extreme rainfall event times be

$$\{t_1^{(i)}, t_2^{(i)}, \ldots, t_{s_i}^{(i)}\} \quad \text{and} \quad \{t_1^{(j)}, t_2^{(j)}, \ldots, t_{s_j}^{(j)}\},$$

where s_i and s_j denote the total numbers of EREs at locations i and j, respectively. For the l-th event at location i and the m-th event at location j, we define the dynamic temporal delay $\tau_{l,m}^{(i,j)}$ as:

$$\tau_{l,m}^{(i,j)} = \min\Big\{\tfrac{1}{2}\big(t_{l+1}^{(i)} - t_l^{(i)}\big),\ \tfrac{1}{2}\big(t_l^{(i)} - t_{l-1}^{(i)}\big),\ \tfrac{1}{2}\big(t_{m+1}^{(j)} - t_m^{(j)}\big),\ \tfrac{1}{2}\big(t_m^{(j)} - t_{m-1}^{(j)}\big)\Big\}. \quad (1)$$

Here, indices $l+1$ or $l-1$ (and similarly $m+1$ or $m-1$) refer to valid neighboring events in time. Events at i and j are deemed synchronized if their occurrence times differ by no more than 10 days (i.e., $|\, t_l^{(i)} - t_m^{(j)}| \leq 10$).

2. Counting directional synchronization

Define a function $J_{l,m}^{(i\leftarrow j)}$ that counts how often an event at j is followed by an event at i:

$$J_{l,m}^{(i\leftarrow j)} \;=\; \begin{cases} 1 & \text{if } 0 < \left(t_l^{(i)} - t_m^{(j)}\right) < \tau_{l,m}^{(i,j)}, \\ 0.5 & \text{if } t_l^{(i)} = t_m^{(j)}, \\ 0 & \text{otherwise.} \end{cases} \tag{2}$$

Summing $J_{l,m}^{(i\leftarrow j)}$ over all event pairs (l, m) gives the count $c(i \mid j)$:

$$c(i \mid j) \;=\; \sum_{l=1}^{s_i} \sum_{m=1}^{s_j} J_{l,m}^{(i\leftarrow j)}. \tag{3}$$

3. Total synchronization strength

We denote the total synchronization strength Q_{ij} between locations i and j as the sum of mutual directional counts:

$$Q_{ij} \;=\; c(i \mid j) \;+\; c(j \mid i). \tag{4}$$

A larger Q_{ij} indicates stronger event synchronization between the two grid cells.

4. Constructing the synchronization matrix

Once ES is applied to all pairs (i, j), we obtain a large synchronization matrix $\mathbf{Q} = \big(Q_{ij}\big)$ of dimension $N \times N$, where N is the total number of grid points. Consecutive events within a small time window at the same location are merged into a single effective event to avoid artifactual counts ($J_{l,m} = 0.5$ for extended blocks).

5. Significance test and adjacency matrix

We assess the statistical significance of Q_{ij} using surrogate event sequences that emulate random timing while preserving the observed number of events at each location. Specifically, under the null hypothesis that e_i and e_j are random and independent, we draw 2,000 pairs of surrogate time series $\{e_i', e_j'\}$, each having the same numbers s_i and s_j of events as the real series. We compute Q_{ij}' for each surrogate pair, yielding an empirical distribution of synchronization strengths. The observed synchronization Q_{ij} is deemed significant at the 95% level if:

$$Q_{ij} \;>\; Q_{ij}'(\alpha = 0.95), \tag{5}$$

where $Q_{ij}'(\alpha = 0.95)$ is the 95th percentile of the surrogate based values.

Let $\boldsymbol{\mathcal{A}} = \big(\mathcal{A}_{ij}\big)$ denote the adjacency matrix. We set

$$\mathcal{A}_{ij} \;=\; \begin{cases} 1 & \text{if } Q_{ij} \text{ is significant,} \\ 0 & \text{otherwise.} \end{cases} \tag{6}$$

Thus, $\mathcal{A}_{ij} = 1$ indicates that EREs at location i follow events at location j (or vice versa) more frequently than expected under purely random conditions, implying a statistically robust link in the event synchronization network.

Lagged Correlation and High Synchronization times Between Europe and South Central Asia

Let Region A (Europe) contain M grid cells, and Region B (South Central Asia) contain N grid cells. On any given day t, we identify the subset of $m(t)$ grid cells in Region A that exceed the 90th percentile threshold for extreme rainfall events (EREs). Denoting daily precipitation at the i-th grid cell in Region A as $E_{A,i}(t)$, we define an indicator:

$$\mathrm{ERE}_{A,i}(t) = \begin{cases} 1, & E_{A,i}(t) \geq q_{A,i}, \\ 0, & \text{otherwise,} \end{cases} \tag{7}$$

where $q_{A,i}$ is the 90th percentile rainfall threshold at grid cell i. Thus,

$$m(t) = \sum_{i=1}^{M} \mathrm{ERE}_{A,i}(t). \tag{8}$$

We then look ahead over a 10 day window ($\tau = 10$) in Region B, summing the total number of grid cells that experience EREs from day t to day $t + \tau$. Let:

$$n(t) = \sum_{\ell=0}^{\tau} \sum_{j=1}^{N} \mathrm{ERE}_{B,j}(t + \ell). \tag{9}$$

Multiplying $m(t)$ and $n(t)$ yields a day-specific measure of synchronized extremes:

$$ES_{A\to B}(t) = m(t) \times n(t). \tag{10}$$

Repeating this calculation over all days t generates the time series $\{ES_{A\to B}(t)\}$. A low pass Chebyshev filter is then applied to smooth short term fluctuations. Reversing the roles of Regions A and B produces $ES_{B\to A}(t)$ following the same procedure. Then we determine days of strong synchronization by identifying the local maxima of the timeseries that are above the 90th percentile of the entire timeseries $\{ES_{A\to B}(t)\}$.

Once we obtain the two synchronization time series, $\{ES_{A\to B}(t)\}$ and $\{ES_{B\to A}(t)\}$, we compute the *Spearman rank correlation* at lags up to ±30 days:

$$\rho_k = \mathrm{SpearmanCorr}\Big(ES_{A\to B}(t),\; ES_{B\to A}(t-k)\Big), \quad k \in [-30, \ldots, 30]. \tag{11}$$

We define the *peak correlation* and corresponding lag:

$$k_{\text{peak}} = \arg\max_k |\rho_k|. \tag{12}$$

PCMCI+

Multivariate time series setup

Consider a multivariate time series

$$\mathbf{X}(t) \;=\; \big(X_1(t),\, X_2(t),\, \ldots,\, X_N(t)\big), \quad t = 1, \ldots, T, \tag{13}$$

where each $X_i(t)$ represents one climate index. We define a maximum lag $\tau_{\max}$ for the time dependencies:

$$\mathcal{P}_i \;=\; \big\{\, (j, \tau) \;\mid\; 1 \le j \le N,\; 1 \le \tau \le \tau_{\max} \big\}, \tag{14}$$

so that for each variable X_i, potential parents or drivers can include $X_j(t\tau)$ for $(j, \tau) \in \mathcal{P}_i$. In our application, we set $\tau_{\max} = 5$ months to allow for sub seasonal to seasonal lead-lag relationships.

Overview of the algorithm

PCMCI+ is a two stage algorithm building on a structural causal framework for momentary conditional independence. Let $\mathbf{X}_t \equiv \mathbf{X}(t)$ for brevity, and write

$$X_{i,t} \equiv X_i(t), \quad X_{j,t-\tau} \equiv X_j(t - \tau).$$

The algorithm aims to identify the set of parents (or direct drivers) of each X_i, denoted $\mathbf{\Pi}_i \subseteq \mathcal{P}_i$. Once $\mathbf{\Pi}_i$ is determined, PCMCI+ evaluates whether $X_{j,t-\tau}$ remains a significant predictor of $X_{i,t}$ when conditioning on other relevant variables and lags.

Step 1: PC stable adjacency selection

1. For each target variable X_i, initialize the adjacency set $\mathbf{A}_i \leftarrow \mathcal{P}_i$.
2. For each order $q = 0, 1, 2, \ldots$:
   (a) For each pair $(i, (j, \tau))$ currently in $\mathbf{A}_i$, test whether

   $$(X_{i,t} \;\perp\; X_{j,t-\tau}) \mid \mathbf{S}$$

   for some subset $\mathbf{S}$ of size q drawn from $\mathbf{A}_i \setminus \{(j, \tau)\}$.
   (b) If a conditional independence test is satisfied (e.g., partial correlation = 0 at a chosen significance level), remove (j, τ) from $\mathbf{A}_i$.
   (c) Continue until no more links can be removed at order q.

The final adjacency sets $\{\mathbf{A}_i\}_{i=1}^{N}$ are then used in the second stage.

Step 2: Momentary Conditional Independence (MCI) test

For each candidate parent $(j, \tau) \in \mathbf{A}_i$, an MCI test checks whether

$$\left(X_{i,t} \;\perp\; X_{j,t-\tau} \mid \mathbf{S}\right), \tag{15}$$

where $\mathbf{S} \subseteq \{\mathbf{X}_{t-1}, \ldots, \mathbf{X}_{t-\tau_{\max}}\} \setminus \{(j, \tau)\}$. In practice, MCI uses a multivariate regression approach that conditions on $\mathbf{S}$. If conditional independence holds, (j, τ) is removed from the parent set of X_i.

Partial correlation based test

For both adjacency selection and MCI, we use the partial correlation (ParCorr) measure to test for conditional independence. Let Y_i and Y_j denote the standardized residuals of $X_{i,t}$ and $X_{j,t-\tau}$ after regressing out the conditioning set $\mathbf{S}$. Then the partial correlation is

$$\rho_{\text{ParCorr}}\left(X_{i,t},\, X_{j,t-\tau} \;\mid\; \mathbf{S}\right) \;=\; \frac{\mathbb{E}[\,Y_i\,Y_j\,]}{\sqrt{\mathbb{E}[\,Y_i^2\,]\,\mathbb{E}[\,Y_j^2\,]}}. \tag{16}$$

Under the null hypothesis of conditional independence, $\rho_{\text{ParCorr}} = 0$. A corresponding test statistic under approximate normality is

$$T \;=\; \rho_{\text{ParCorr}} \sqrt{\frac{|\mathbf{D}| - |\mathbf{S}| - 2}{1 - \rho^2_{\text{ParCorr}}}}, \tag{17}$$

where $|\mathbf{D}|$ is the sample size and $|\mathbf{S}|$ is the size of the conditioning set. A threshold on T (or its p-value) determines rejection of the independence hypothesis.

Implementation details

After the MCI step, the final parent sets $\{\mathbf{\Pi}_i\}_{i=1}^{N}$ are refined to remove potential orientation conflicts and form a directed causal graph, where $X_{j,t-\tau} \to X_{i,t}$ indicates a significant lagged influence of index j on index i. In this study, we use a uniform $\tau_{\max} = 5$ months and a nominal 5% significance level for the ParCorr based tests. The algorithm is implemented via the `tigramite` Python package, which provides efficient functions for PCMCI+ inference. By comparing the resulting graphs across our 10 initial condition runs, we assess how ocean-monsoon coupling (e.g., ENSO → ISMR) may vary and whether slower oceanic feedbacks disrupt otherwise stable rainfall teleconnections.

Network Measures

To quantify the properties of the network, we use the following measures:

- **Degree Centrality (DC):** For a network with N nodes, the degree centrality of a node j measures the number of connections (edges) it has:

$$\mathrm{DC}_j = \frac{\sum_{i=1}^{N-1} A_{ij}}{N-1} \tag{18}$$

- **Average Link Length (ALL):** The average link length measures the average physical distance between connected nodes. It is computed as:

$$\mathrm{ALL} = \frac{\sum_{i=1}^{N-1} A_{ij} d_{ij}}{\sum_{i=1}^{N-1} A_{ij}} \tag{19}$$

  where d_{ij} is the physical distance between grid points i and j.

Code availability

PCMCI+ code is obtained from tigramite package available from (https://jakobrunge.github.io/tigramite software.

Acknowledgements

This research was primarily funded by IIT Gandhinagar. UB acknowledges SERB CRG grant (CRG/2023/001438):"Network-of-Network Lens to quantify structural and dynamical aspects of resilience of coupled infrastructure systems", and Monsoon Mission III grant "Improving short-to-medium range extreme precipitation forecasts with Climate Networks and hybrid physics-ML convection parameterization". The authors also thank the members of the Machine Intelligence and Resilience Laboratory at IIT Gandhinagar for their valuable discussions and constructive feedback on this manuscript.

Author contributions

Conceptualization: HP,UB
Analysis: HP, UB
Visualization: HP,UB
Writing original draft: HP,UB,DP
Writing review and editing: HP,UB,DP,AN,RM.

Competing interests

The authors declare no competing interests.

Acknowledgement

References

[1] Deser, C., Knutti, R., Solomon, S. & Phillips, A. S. Communication of the role of natural variability in future north american climate (2012).

[2] Gupta, K. Urban flood resilience planning and management and lessons for the future: a case study of mumbai, india. Urban Water Journal **4**, 183–194 (2007).

[3] Kale, V. On the link between extreme floods and excess monsoon epochs in south asia. Climate dynamics **39**, 1107–1122 (2012).

[4] Kaiser, Z. A. & Akter, F. From risk to resilience and sustainability: Addressing urban flash floods and waterlogging. Risk Sciences 100011 (2025).

[5] Fekete, A. Critical infrastructure and flood resilience: Cascading effects beyond water. Wiley Interdisciplinary Reviews: Water **6**, e1370 (2019).

[6] Bhatia, U. & Ganguly, A. R. Reducing the irreducible uncertainty in return periods of 21st-century precipitation extremes. Scientific Reports **9**, 1–10 (2019).

[7] Upadhyay, D., Mohapatra, P. & Bhatia, U. Depth-duration-frequency of extreme precipitation events under internal climate variability: Indian summer monsoon. Journal of Geophysical Research: Atmospheres **126**, e2020JD034193 (2021).

[8] Hawkins, E. & Sutton, R. The potential to narrow uncertainty in regional climate predictions. Bulletin of the American Meteorological Society **90**, 1095–1107 (2009).

[9] Dai, A. & Bloecker, C. E. Impacts of internal variability on temperature and precipitation trends in large ensemble simulations by two climate models. Climate Dynamics **52**, 289–306 (2019).

[10] Lehner, F., Deser, C., Simpson, I. R. & Terray, L. Attributing the u.s. southwest's recent shift into drier conditions (2018).

[11] Kirchmeier-Young, M. C. & Zhang, X. Human influence has intensified extreme precipitation in north america. Proceedings of the National Academy of Sciences **117**, 13308–13313 (2020).

[12] Knutson, T. R. & Zeng, F. Model assessment of observed precipitation trends over land regions: Detectable human influences and possible low bias in model trends. Journal of Climate **31**, 4617–4637 (2018).

[13] McKinnon, K. A. & Deser, C. The inherent uncertainty of precipitation variability, trends, and extremes due to internal variability, with implications for western u.s. water resources. Journal of Climate **34**, 9605 – 9622 (2021). URL https://journals.ametsoc.org/view/journals/clim/34/24/JCLI-D-21-0251.1.xml.

[14] Pendergrass, A. G. et al. Precipitation variability increases in a warmer climate. Scientific Reports **7**, 17966 (2017).

[15] Blánusa, T. et al. Partitioning climate projection uncertainty with multiple large ensembles and cmip5/6. Earth System Dynamics **11**, 491–508 (2020).

[16] Mondal, S., Mishra, A. K. & Leung, L. R. Spatiotemporal characteristics and propagation of summer extreme precipitation events over united states: A complex network analysis. Geophysical Research Letters **47** (2020).

[17] Tantary, D. et al. Geographical trapping of synchronous extremes amidst increasing variability of indian summer monsoon rainfall. Geophysical Research Letters **50**, e2023GL104788 (2023).

[18] Boers, N., Bookhagen, B., Marwan, N., Kurths, J. & Marengo, J. Complex networks identify spatial patterns of extreme rainfall events of the south american monsoon system. Geophysical Research Letters **40**, 4386–4392 (2013).

[19] Malik, N., Bookhagen, B., Marwan, N. & Kurths, J. Analysis of spatial and temporal extreme monsoonal rainfall over south asia using complex networks. Climate Dynamics **39**, 971–987 (2012).

[20] Boers, N. et al. Complex networks reveal global pattern of extreme-rainfall teleconnections. Nature **566**, 373–377 (2019).

[21] Liu, L., Gao, C., Zhu, Z., Zhang, S. & Tang, X. Spatiotemporal evolution patterns and underlying formation mechanisms of monsoon rainfall across eastern china: A complex network perspective. Atmospheric Research **304**, 107363 (2024).

[22] Nowack, P., Runge, J., Eyring, V. & Haigh, J. D. Causal networks for climate model evaluation and constrained projections. Nature communications **11**, 1415 (2020).

[23] Goswami, B. N., Chakraborty, D., Rajesh, P. V. & Mitra, A. Predictability of south-asian monsoon rainfall beyond the legacy of tropical ocean global atmosphere program (toga). npj Climate and Atmospheric Science **5** (2022).

[24] Chauhan, T., Chandel, V. & Ghosh, S. Global land drought hubs confounded by teleconnection hotspots in equatorial oceans. npj Climate and Atmospheric Science **7** (2024).

[25] Kumar, D. & Ganguly, A. R. Intercomparison of model response and internal variability across climate model ensembles. Climate dynamics **51**, 207–219 (2018).

[26] Strnad, F. M., Schlör, J., Geen, R., Boers, N. & Goswami, B. Propagation pathways of indo-pacific rainfall extremes are modulated by pacific sea surface temperatures. Nature Communications **14** (2023).

[27] Strnad, F., Hunt, K. M. R., Boers, N. & Goswami, B. Intraseasonal synchronization of extreme rainfalls between north india and the sahel (2024). URL http://arxiv.org/abs/2405.08492.

[28] Su, Z., Meyerhenke, H. & Kurths, J. The climatic interdependence of extreme-rainfall events around the globe. Chaos: An Interdisciplinary Journal of Nonlinear Science **32** (2022).

[29] Steinhaeuser, K., Chawla, N. V. & Ganguly, A. R. Complex networks as a unified framework for descriptive analysis and predictive modeling in climate science. Statistical Analysis and Data Mining: The ASA Data Science Journal **4**, 497–511 (2011).

[30] Kornhuber, K. et al. Extreme weather events in early summer 2018 connected by a recurrent hemispheric wave-7 pattern. Environmental Research Letters **14**, 054002 (2019).

[31] Hoskins, B. The potential for skill across the range of the seamless weather-climate prediction problem: a stimulus for our science. Quarterly Journal of the Royal Meteorological Society **139**, 573–584 (2013).

[32] Ding, Q. & Wang, B. Circumglobal teleconnection in the northern hemisphere summer. Journal of climate **18**, 3483–3505 (2005).

[33] Ding, Q. & Wang, B. Intraseasonal teleconnection between the summer eurasian wave train and the indian monsoon. Journal of Climate **20**, 3751–3767 (2007).

[34] Boers, N. et al. Complex networks reveal global pattern of extreme-rainfall teleconnections. Nature **566**, 373–377 (2019).

[35] Nikumbh, A. C., Thakur, A. B. S., Chakraborty, A., Bhat, G. S. & Sukhatme, J. The role of the north atlantic blocking high during large-scale heavy rainfall events over central india. Journal of the Atmospheric Sciences **80**, 1815–1827 (2023).

[36] Rodwell, M. & Hoskins, B. Monsoons and the dynamics of deserts. Quarterly Journal of the Royal Meteorological Society **122**, 1385–1404 (1996).

[37] Yihui, D. & Chan, J. C. The east asian summer monsoon: an overview. Meteorology and Atmospheric Physics **89**, 117–142 (2005).

[38] Parthasarathy, B., Munot, A. & Kothawale, D. All-india monthly and seasonal rainfall series: 1871–1993. Theoretical and Applied Climatology **49**, 217–224 (1994).

[39] Hirahara, S., Ishii, M. & Fukuda, Y. Centennial-scale sea surface temperature analysis and its uncertainty. Journal of Climate **27**, 57–75 (2014).

[40] Slivinski, L. C. et al. Towards a more reliable historical reanalysis: Improvements for version 3 of the twentieth century reanalysis system. Quarterly Journal of the Royal Meteorological Society **145**, 2876–2908 (2019).

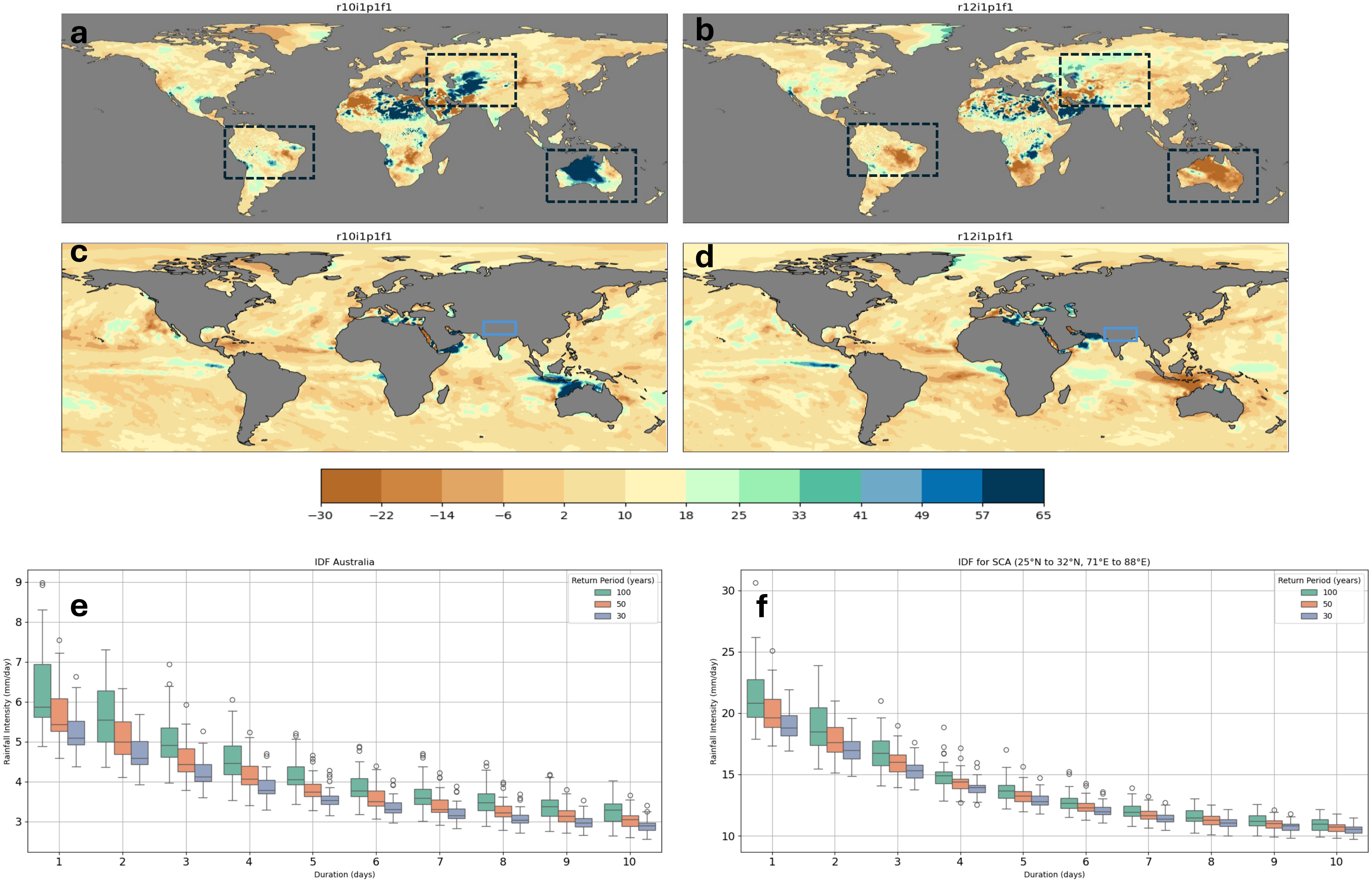
r10i1p1f1
a
r12i1p1f1
b
r10i1p1f1
c
r12i1p1f1
d
−30
−22
−14
−6
2
10
18
25
33
41
49
57
65
IDF Australia
e
Return Period (years)
100
50
30
Rainfall Intensity (mm/day)
9
8
7
6
5
4
3
1
2
3
4
5
6
7
8
9
10
Duration (days)
IDF for SCA (25°N to 32°N, 71°E to 88°E)
f
Return Period (years)
100
50
30
Rainfall Intensity (mm/day)
30
25
20
15
10
1
2
3
4
5
6
7
8
9
10
Duration (days)

Fig. 1: Spatial change in JJAS precipitation and IDF characteristics across ICs. Panels (a) and (b) show the percentage change in mean JJAS precipitation between the recent (1981–2010) and historical (1951–1980) climatology over land for two randomly selected ICs (r10i1p1f1 and r12i1p1f1, respectively) from the EC-Earth3 historical ensemble. Dashed boxes highlight regions with stark contrasts: the Amazon, South Asia, and Australia. Panels (c) and (d) depict the same analysis as (a) and (b), respectively, but over the ocean. Panels (e) and (f) present Intensity-Duration-Frequency (IDF) curves for Australia and South Central Asia (SCA: 25°N to 32°N, 71°E to 88°E), respectively. Return levels for 30 , 50 , and 100 year periods are estimated using the block maxima approach and fitted with the Generalized Extreme Value (GEV) distribution. The boxplots summarize the spread across 50 initial condition ensemble members.

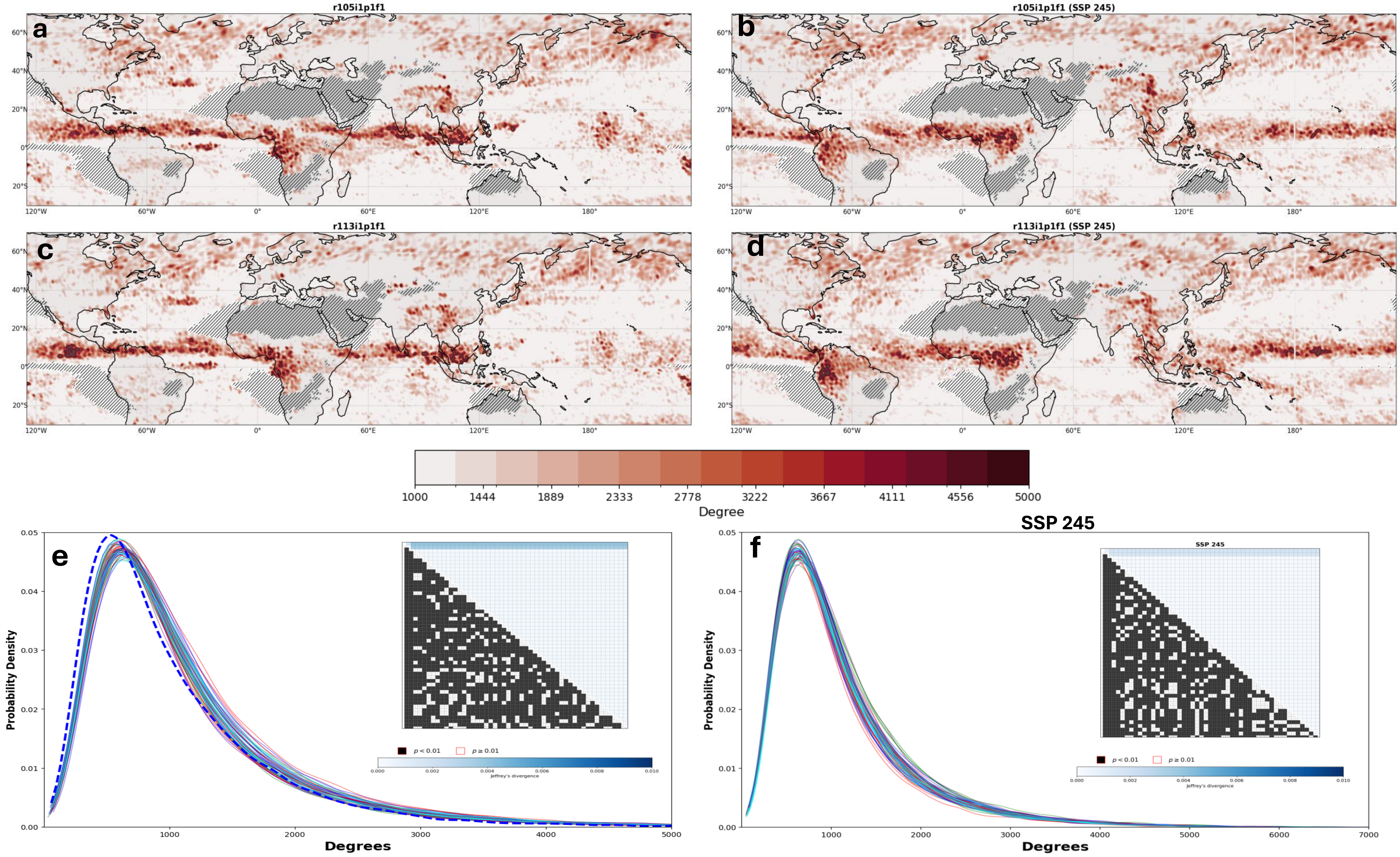
a
r105i1p1f1
b
r105i1p1f1 (SSP 245)
c
r113i1p1f1
d
r113i1p1f1 (SSP 245)
60°N
40°N
20°N
0°
20°S
120°W
60°W
0°
60°E
120°E
180°
1000
1444
1889
2333
2778
3222
3667
4111
4556
5000
Degree
e
SSP 245
f
Probability Density
Degrees
0.00
0.01
0.02
0.03
0.04
0.05
1000
2000
3000
4000
5000
6000
7000
$p < 0.01$
$p \geq 0.01$
0.000
0.002
0.004
0.006
0.008
0.010
Jeffrey's divergence
SSP 245

Fig. 2: Spatial and statistical analysis of degree distributions from historical and future simulations. Panels (a) and (b) display the spatial distribution of network degree for one selected initial condition (r105i1p1f1) from the EC Earth3 ensemble. Panel (a) corresponds to the network constructed from the historical simulation (1980-2014), while panel (b) corresponds to the network constructed from the SSP245 scenario (2015-2049). Panels (c) and (d) show the same for another initial condition (r113i1p1f1). Hatched regions indicate areas with fewer than five EREs and are excluded from the analysis. Panel (e) shows the empirical probability density functions (PDFs) of node degree across 50 networks derived from 50 ICs under the historical scenario. The thick blue dashed line represents the KDE of the degree distribution from the observational MSWEP dataset for the same period. The inset in panel (e) includes a matrix where the lower triangle displays the results of pairwise Kolmogorov Smirnov (KS) tests at the 0.01 significance level black cells denote pairs of networks not significantly different while the upper triangle shows the corresponding Jeffreys divergence values. Panel (f) shows the same analysis as (e), but for networks constructed from the SSP 245 scenario (2015-2049).

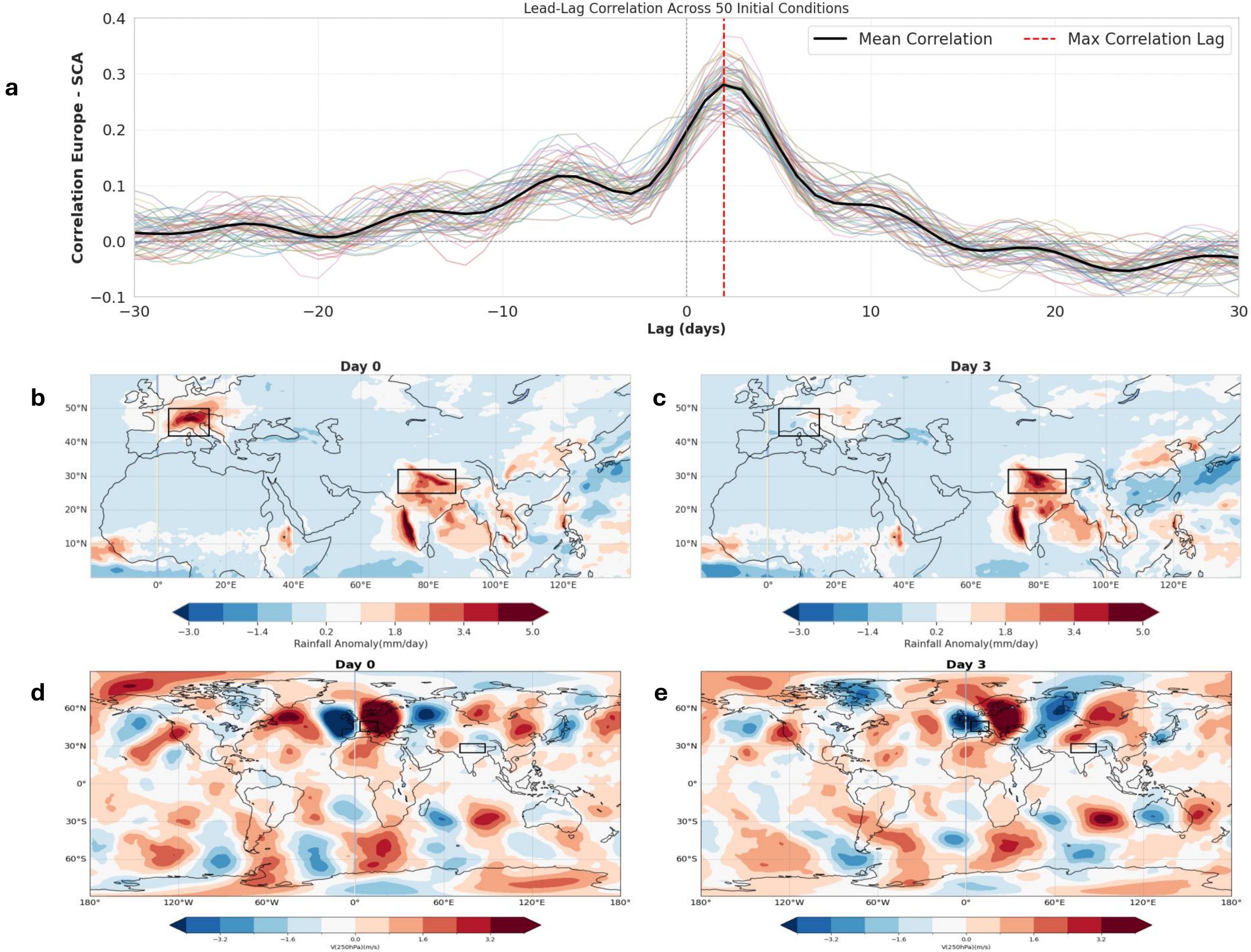
a
Lead-Lag Correlation Across 50 Initial Conditions
Correlation Europe - SCA
Lag (days)
Mean Correlation
Max Correlation Lag
0.4
0.3
0.2
0.1
0.0
−0.1
−30
−20
−10
0
10
20
30
b
Day 0
c
Day 3
50°N
40°N
30°N
20°N
10°N
0°
20°E
40°E
60°E
80°E
100°E
120°E
−3.0
−1.4
0.2
1.8
3.4
5.0
Rainfall Anomaly(mm/day)
d
Day 0
e
Day 3
60°N
30°N
0°
30°S
60°S
180°
120°W
60°W
0°
60°E
120°E
180°
−3.2
−1.6
0.0
1.6
3.2
V(250hPa)(m/s)

Fig. 3: Lead–lag relationships and composite rainfall anomalies between Europe and South Central Asia (SCA). Panel (a) shows the lead–lag correlation between Europe (42°N–50°N, 3°E–15°E) and South Central Asia (SCA) based on spatially aggregated daily counts of EREs above the 90th percentile. All time series are smoothed using an 10-day low pass filter (see Methods: 'Lagged Correlation and High Synchronization Times Between Europe and South Central Asia'). Colored lines correspond to individual ICs, while the A thick solid black line shows the ensemble mean correlation across 50 ICs. The dashed The red line indicates the lag at which the mean correlation peaks. Panels (b) and (c) for IC 105 display composite rainfall anomalies on day 0 and day 3, respectively, for days with high numbers of EREs in Europe followed by associated EREs in SCA. Panels (d) and (e) show the Composite anomalies of the meridional wind component v at 250 hPa. Anomalies are expressed in mm/day for rainfall and m/s for V at 250 hPa, and black boxes highlight the Europe and SCA regions used for analysis.The wave train strengthens towards the east within 3 days after the initial ERE occurrence in Europe. The dominant wavenumber associated with this Rossby wave pattern is 6, determined from the spatial power spectral density of the latitude belt from 37.5° N to 47.5° N.

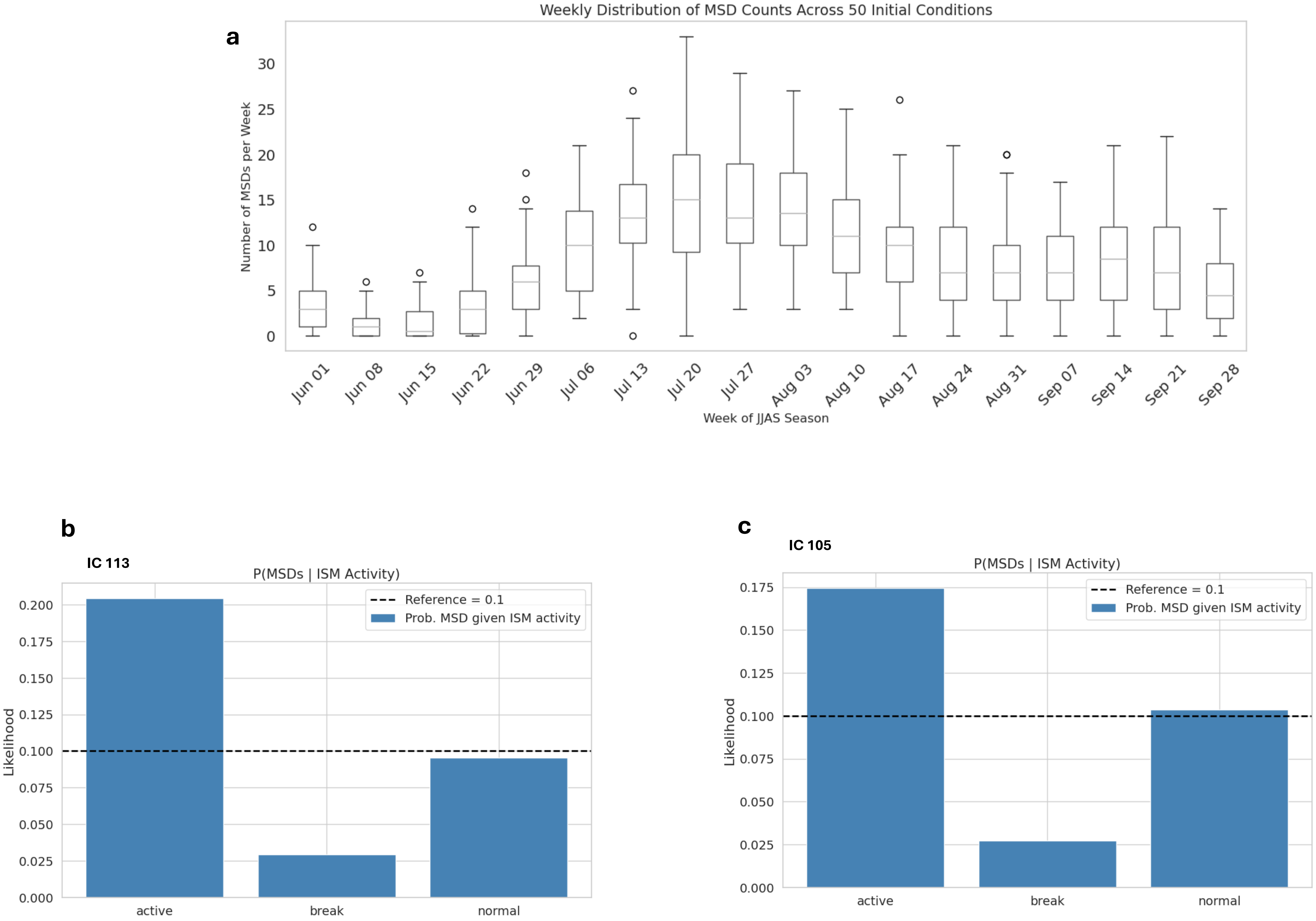
a
Weekly Distribution of MSD Counts Across 50 Initial Conditions
Number of MSDs per Week
0
5
10
15
20
25
30
Jun 01
Jun 08
Jun 15
Jun 22
Jun 29
Jul 06
Jul 13
Jul 20
Jul 27
Aug 03
Aug 10
Aug 17
Aug 24
Aug 31
Sep 07
Sep 14
Sep 21
Sep 28
Week of JJAS Season
b
IC 113
P(MSDs | ISM Activity)
Reference = 0.1
Prob. MSD given ISM activity
Likelihood
0.000
0.025
0.050
0.075
0.100
0.125
0.150
0.175
0.200
active
break
normal
c
IC 105
P(MSDs | ISM Activity)
Reference = 0.1
Prob. MSD given ISM activity
Likelihood
0.000
0.025
0.050
0.075
0.100
0.125
0.150
0.175
active
break
normal

Fig. 4: Distribution of Synchronous days over week of year for the 50 ICs and ,likelihood of MSDs based on ISM activity. (a) For the MSDs, we estimate the distribution over the week of the year in the JJAS observation period for all the initial condition which peak around july and august. (b) and (c) The occurrence of MSDs is conditioned on the Indian summer monsoon phases for IC 105 and IC 113.

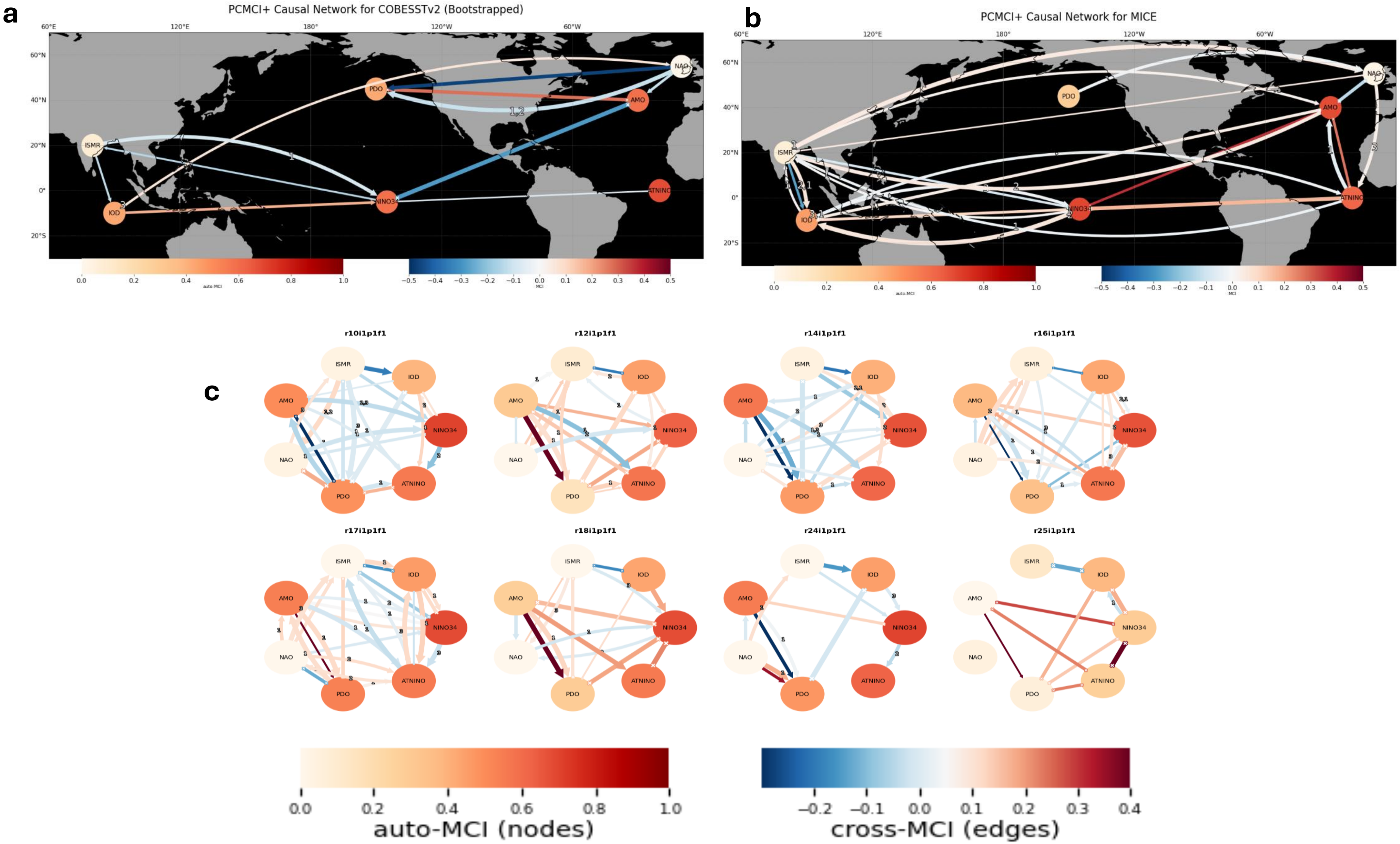
a
PCMCI+ Causal Network for COBESSTv2 (Bootstrapped)
60°E
120°E
180°
120°W
60°W
60°N
40°N
20°N
0°
20°S
NAO
PDO
AMO
ISMR
NINO34
ATNINO
IOD
auto-MCI
MCI
b
PCMCI+ Causal Network for MICE
c
r10i1p1f1
r12i1p1f1
r14i1p1f1
r16i1p1f1
r17i1p1f1
r18i1p1f1
r24i1p1f1
r25i1p1f1
0.0
0.2
0.4
0.6
0.8
1.0
auto-MCI (nodes)
−0.2
−0.1
0.0
0.1
0.2
0.3
0.4
cross-MCI (edges)

Fig. 5: Causal Networks among Major Climate Modes and Indian Summer Monsoon Rainfall (ISMR). Panels (a–b) illustrate causal relationships among major climate indices—Indian Ocean Dipole (IOD), El Niño–Southern Oscillation (ENSO; NINO3.4), Atlantic Multidecadal Oscillation (AMO), North Atlantic Oscillation (NAO), Pacific Decadal Oscillation (PDO), Atlantic Niño (ATLNINO) and ISMR, determined using PCMCI+. Panel (a) shows results derived from observational data (COBE SST anomalies and IMD rainfall, 1871–2014), while panel (b) presents the ensemble concatenated network across eight ICs from the EC Earth3 historical runs (1850–2014). Panel (c) displays networks for individual EC Earth3 ICs. Arrows indicate causal directions: red (positive), blue (negative), with curved arrows showing lagged causal links (lags labeled in months) and straight arrows showing contemporaneous links. Node colors reflect self dependency strength (auto MCI). Link widths correspond to the frequency of each causal relationship identified through bagging (200 repetitions).

Supplementary Information

Robust networks of rainfall extremes emerge despite fragile ocean monsoon causality under Internal variability

This file includes:

Supplementary Figures S1 to S5

1. Global connectivity structure for piControl simulation

To establish a reference for the spatial connectivity of rainfall extremes in the absence of external forcing, we applied the event synchronization method as described in the main text to a 35-year subset of the pre-industrial control (piControl) simulation. This analysis mirrors the procedure previously performed on the 50 initial-condition ensemble members of EC-Earth3, yielding nearly identical network metrics. The congruence between the piControl and ensemble-based results implies that the large-scale organization of rainfall extreme events is predominantly shaped by internal climate variability, rather than by model initialization or transient forcings. Consequently, the piControl-derived network structures serve as robust baselines for assessing changes in extreme-rainfall connectivity under anthropogenic influences.

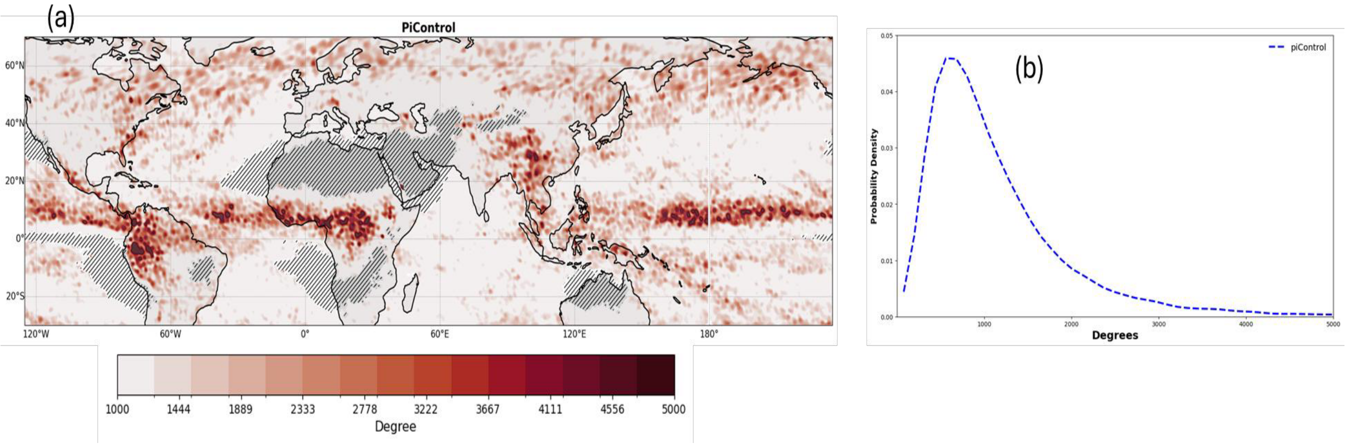

Supplementary Figure S1.

Spatial and statistical analysis of degree distributions from piControl simulations forEarth system models: EC-Earth3 (a) display the spatial distribution of network degree (b) shows the empirical probability density functions (PDFs) of node degree of networks derived from piControl simulations.

2. Invariance of Global connectivity structure of Rainfall extremes for historical simulation

We applied the event-synchronization method to extreme rainfall events identified in each of 50 initial-condition ensemble members of EC-Earth3 under historical forcing (1980–2014). Despite different initial states, the derived network topology remained essentially identical across all realizations. We attribute this invariance to the small variation in the number of extreme events across ensemble members. To demonstrate this, we computed, at each grid cell, the ensemble mean and standard deviation of extreme-event counts over the 50 simulations: the mean map highlights the spatial distribution of extreme-rainfall events frequency, while the low values in the standard-deviation map confirm that extreme-event occurrence is remarkably consistent across different initial conditions.

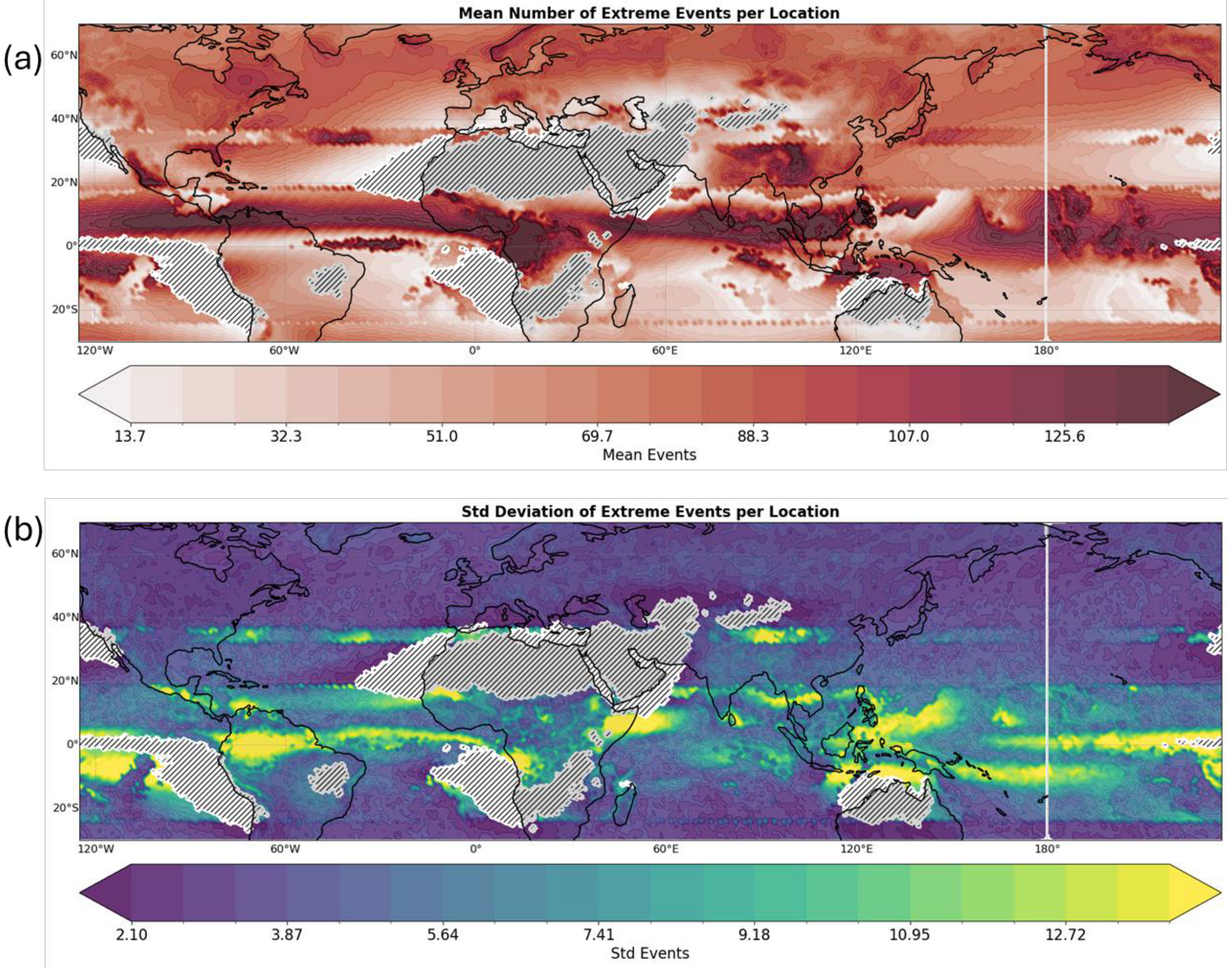

Supplementary Figure S2. (a) Ensemble means number of extreme rainfall events per grid cell across 50 EC-Earth3 initial-condition members for 1980–2014. (b) Corresponding standard deviation of extreme-event counts, illustrating the low variability in extreme-rainfall frequency across the ensemble.

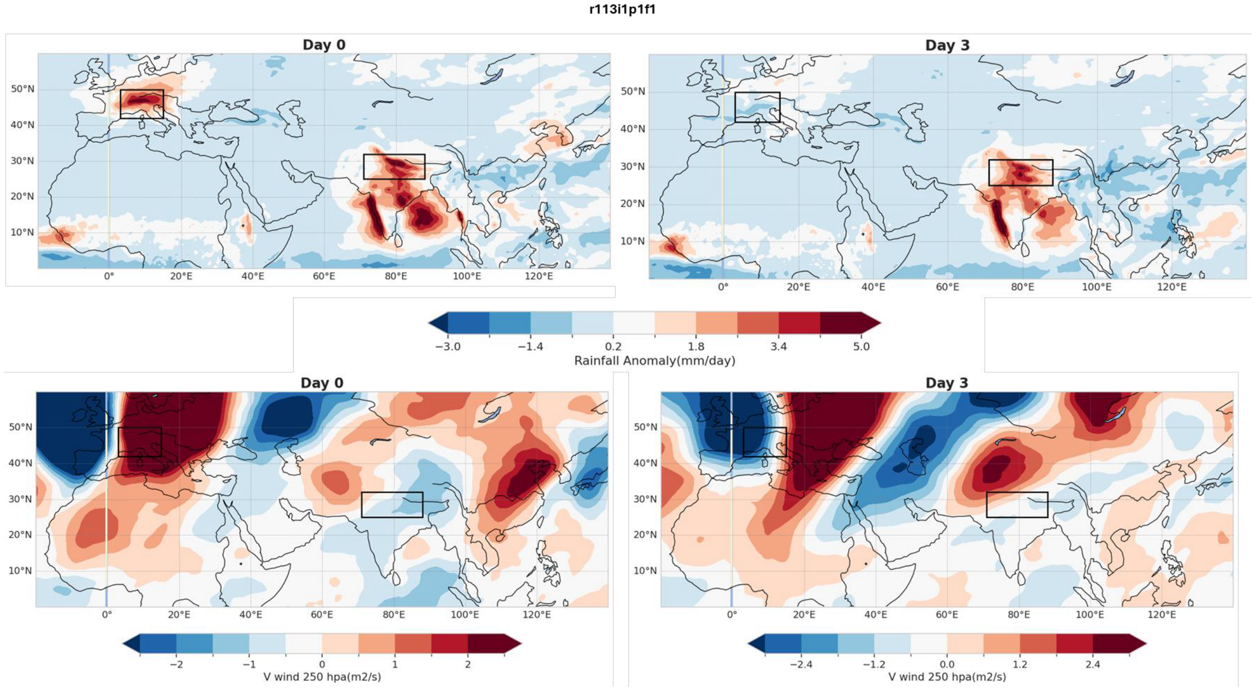

Supplementary Figure S3

Same as Main text Figure 3 but for IC 113

Top panel shows the Composite rainfall anomalies on day 0 and day 3, respectively, for days with high numbers of EREs in Europe followed by associated EREs in SCA.bottom panels show the Composite anomalies of the meridional wind component v at 250 hPa. Anomalies are expressed in mm/day for rainfall and m/s for V at 250 hPa, and black boxes highlight the Europe and SCA regions used for analysis.The wave train strengthens towards the east within 3 days after the initial ERE occurrence in Europe. The dominant wavenumber associated with this Rossby wave pattern is 6, determined from the spatial power spectral density of the latitude belt from 37.5° N to 47.5° N.

Supplementary Figure S4

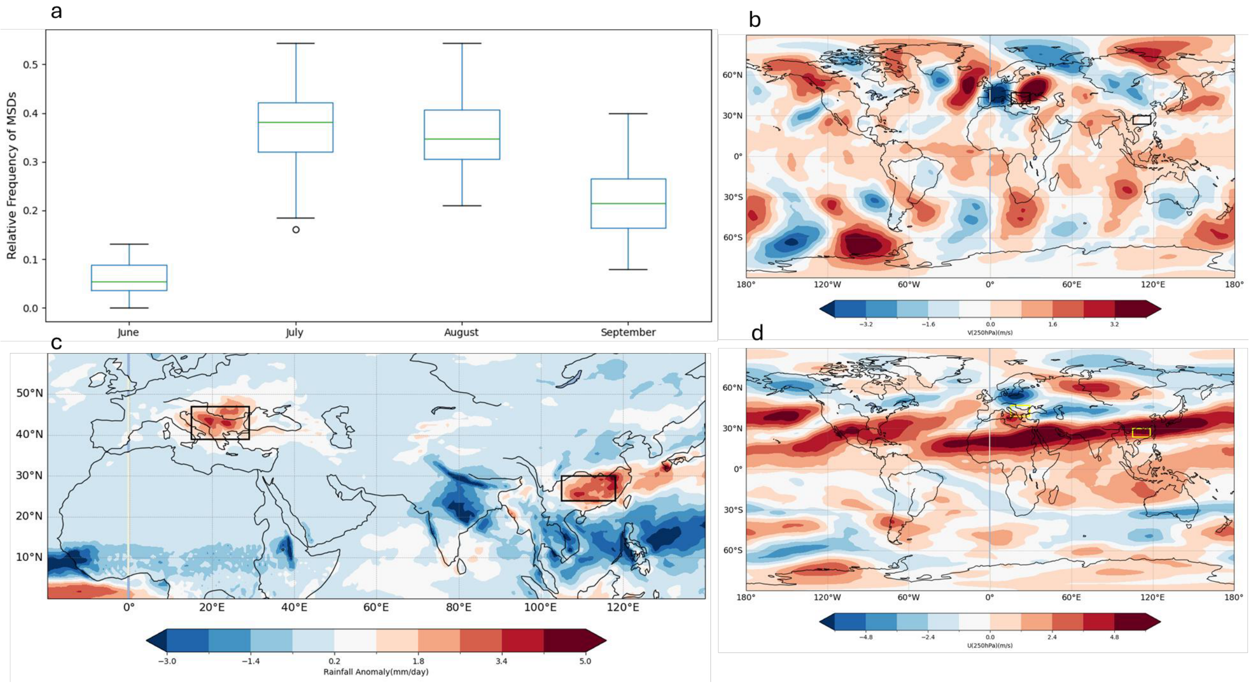

Atmospheric conditions for the teleconnection pattern between South-East Europe and South China, marked with boxes. (a) Frequency of days when these regions are highly synchronized over JJAS across all 50 initial conditions. (b) and (d) Composite anomalies of 250 hPa meridional wind component V and 250 hPa zonal wind component u, with respect to the JJAS climatology, (c) Composite anomalies of Rainfall with respect to the JJAS climatology when South-East Europe and South China are highly synchronised for the IC 105.(see Sec. **Lagged Correlation and High Synchronization times Between Europe and South Central Asia** in main for identification of Most synchronous days).

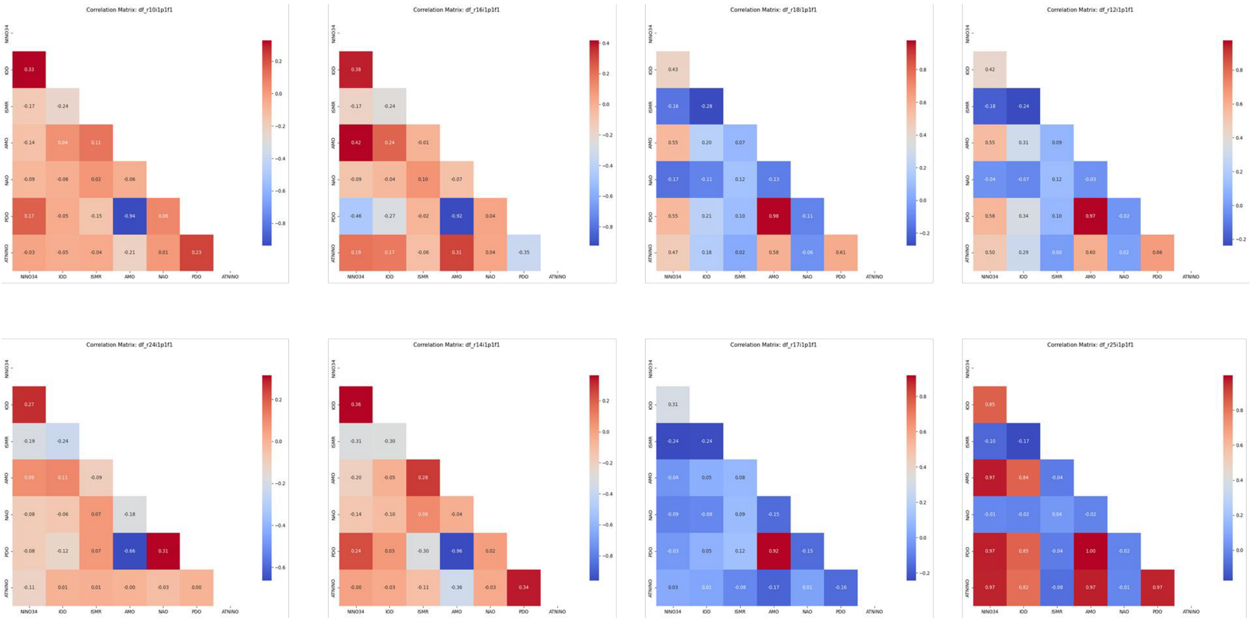

Supplementary Figure S5. To evaluate how different initial-condition realizations affect the inferred causal relationships among key climate modes, we computed the Pearson correlation for eight selected EC-Earth3 ensemble members. Each matrix element represents the correlation between the two nodes NINO34, IOD, ISMR, AMO, NAO, PDO, and ATNINO over the same period for which the PCMCI network has been constructed in Main text fig 5.